Journal of Materials Chemistry A

PAPER

View Article Online
View Journal | View Issue

Cite this: J. Mater. Chem. A, 2016, 4, 15049

Ni@NiO core/shell dendrites for ultra-long cycle life electrochemical energy storage†

Yan Liu,[a] Nianqing Fu,[a] Guoge Zhang,[b] Wei Lu,[a] Limin Zhou[c] and Haitao Huang*[a]

Received 1st July 2016
Accepted 22nd August 2016

DOI: 10.1039/c6ta05508g

www.rsc.org/MaterialsA

A dendritic Ni@NiO core/shell electrode (DNE) is successfully fabricated by electrodeposition in a Ni-free electrolyte, with a Ni anode providing Ni ions through dissolution and diffusion. The unique structure is ideal for electrochemical energy storage since the dendrites provide a large surface area for easy electrolyte infiltration; the metal core improves the electrode conductivity with a shortened ion diffusion path, and the metal oxide shell is active for faradaic charge storage. As a result, the synthesized DNE demonstrates a high specific capacitance of 1930 F g^{-1} and a high areal capacitance of 1.35 F cm^{-2}, with super-long cycle stability. The gravimetric capacitance of the DNE hardly shows any decay after 70 000 cycles at a scan rate of 100 mV s^{-1}. It was also demonstrated that our electrodeposition method in a source-free electrolyte is universal to deposit dendritic Ni-compounds on many other types of substrates, versatile for different applications.

Introduction

Electrochemical energy storage devices (EESDs) have attracted vast attention in recent years.[1] Nickel based materials have been identified as promising electrode materials for electrochemical energy storage devices because of their high theoretical specific capacitance (~2584 F g^{-1} for NiO and 2082 F g^{-1} for $Ni(OH)_2$), environmental friendliness and low cost.[2,3] With the aim to provide a larger reaction area and shorten ion diffusion paths, many fabrication methods including chemical precipitation,[4,5] hydrothermal synthesis,[6–11] sol–gel,[12,13] thermal oxidation[14–16] and anodization[17,18] have been used to produce various kinds of nickel-based nanostructures, such as amorphous $Ni(OH)_2$ nanoboxes,[5] Ni–Co oxide nanowires,[6,19] $Ni(OH)_2$ nanosheets,[7,11] NiO nanobelts,[8] nanosized rambutan-like NiO,[9] urchin-like $NiCo_2O_4$,[10] spinel nickel cobaltite aerogels,[12] NiO nanoflowers,[13] NiO nanoblocks[14] and sponge-like $Ni(OH)_2$–NiF_2 composites.[18] Apart from the above methods, electrodeposition has gained more and more attention because the electroactive material can be directly grown on a current collector without the need for using any binder or conducting agent.[20] Flaky Ni_3S_2 (ref. 21) 3D concentration-gradient nickel–cobalt hydroxide nanostructures,[22] nickel–cobalt hydroxide nano-networks,[23] NiO nanotube based interconnected NiO nanoflakes,[24] and ternary Ni–Co–Cu oxyhydroxide nanosheets[25] have been successfully synthesized by electrodeposition and proved promising for EESDs. However, most of the electrodeposited nickel-based materials are in the form of nanoflakes or agglomerated nanoparticles, which lead to low specific surface areas (<30 m^2 g^{-1}) and limited specific capacitances (<1000 F g^{-1}).[26] Another problem facing the nickel-based electrode material is its low electrical conductivity, which not only restricts the power performance but also prevents the utilization of thick electrodes.[2,24] One feasible approach to this problem is to electrodeposit nanosized active materials over a 3D conductive framework to form hybrid nanostructures, such as coaxial $Ni_xCo_{2x}(OH)_{6x}$/TiN nanotube arrays,[20] hierarchical TiN@$Ni(OH)_2$ core/shell nanowire arrays,[27] and ITO/NiO nanowires.[28] Both the specific capacitance and power density can be improved as expected. However, the adhesion strength between the electrodeposited material and the nanostructured current collector is relatively weak, leading to an inferior cycle life (for example, ~30% capacitance retention after 200 cycles[27] and 7.3% capacitance loss after 500 cycles[28]). Moreover, the preparation of 3D conductive networks complicates the processing procedure and impairs the electrode fabrication efficiency.[20] Hence, it is still challenging to prepare nickel-based electrodes with both high capacity and excellent stability by electrodeposition.

Here we report a novel electrodeposition method by using a source-free electrolyte. A Ni anode acts as the source to provide a stable and low Ni ion concentration through dissolution and diffusion, which results in a low nucleation rate and anisotropic growth of a novel core/shell structured dendritic Ni@NiO electrode (DNE). The well aligned dendritic structure facilitates electrolyte penetration. The metallic Ni core provides efficient electron transport and greatly shortens the ion diffusion path in

[a]Department of Applied Physics and Materials Research Center, The Hong Kong Polytechnic University, Hung Hom, Kowloon, Hong Kong, China. E-mail: aphhuang@polyu.edu.hk

[b]School of Materials Science and Engineering, South China University of Technology, Guangzhou, 510640, P. R. China

[c]Department of Mechanical Engineering, The Hong Kong Polytechnic University, Hung Hom, Kowloon, Hong Kong, China

† Electronic supplementary information (ESI) available: Section A for calculation; Section B (Fig. S1–S18) for supplementary figures. See DOI: 10.1039/c6ta05508g

the NiO shell. A high specific capacitance of 1930 F g^{-1} is achieved at a current density of 2.9 A g^{-1} (areal capacitance $\sim$ 1.35 F cm^{-2}), with a super-long cycle life (no capacitance decay after 70 000 charge/discharge cycles). The power density is greatly enhanced, compared with other electrodeposited nickel-based materials.[2,29] The technique reported here has been shown to be effective in the electrodeposition of similar microstructures on various types of substrates.

Experimental

Materials preparation

All chemicals were of analytical reagent grade, and used as received. Prior to the experiment, nickel foils (0.2 mm in thickness, 99.6% in purity, Yirun Pte. Ltd., China) were degreased ultrasonically in acetone and ethanol, respectively, for 30 min, followed by washing with de-ionized (DI) water and drying in hot air. The electrodeposition of active materials was carried out by using a DC power supply (N5751A, Agilent Technologies Ltd, US) in unstirred ethylene glycol (EG) electrolyte containing NH_4F (0.1% w/w) and DI water (3% v/v), with two nickel foils (0.5 $\times$ 4 cm^2) as the anode and cathode, respectively. The foils were subjected to potentiostatic electrodeposition at 60 V for 60 min. All the experiments were carried out at 40 °C in a controlled thermostat water bath. The deposited cathodic electrodes were soaked in ethanol for 2 hours and then rinsed with DI water, followed by drying in hot air.

Characterization

A scanning electron microscope (SEM, TM 3000, Hitachi, Japan) and a transmission electron microscope (TEM, JOEL JEM-2010, Japan) were used to characterize the microstructure. Energy dispersive spectroscopy (EDS) was employed to analyze the sample composition. X-ray diffraction (XRD, Rigaku D/max IIIA, Cu kα, λ = 0.15418 nm, Japan) was performed to examine the crystalline structure. The scraped-off powders of the DNE were used for the above measurements. Raman spectra were taken on a HORIBA HR800 Raman spectrometer at 488 nm. X-Ray photoelectron spectroscopy (XPS, Thermo Microlab 350) measurements were employed to study the surface composition of the DNE material inside an ultrahigh vacuum chamber. Electrochemical characterizations, such as cyclic voltammetry (CV), galvanostatic charge/discharge (GCD) and electrochemical impedance spectroscopy (EIS, 5 mV amplitude, 0.01–10 kHz frequency range), were carried out by using an electrochemical workstation (CHI660e) in 1 mol L^{-1} NaOH with a three-electrode system. Platinum was used as the counter electrode, and a saturated calomel electrode (SCE) was used as the reference electrode.

Results and discussion

In our method (Scheme 1), at the beginning of electrodeposition, the Ni^{2+} mainly came from the field-assisted anodic dissolution of Ni foil, $Ni - 2e^- \rightarrow Ni^{2+}$, which provided the slow nucleation and growth of nickel and nickel oxide/hydroxide on the cathode. When Ni^{2+} ions arrived at the cathode surface *via* diffusion and electric field driven migration, Ni nucleated and grew, involving the reactions $Ni^{2+} + 2e^- \rightarrow Ni$, $Ni^{2+} + 2OH^- \rightarrow Ni(OH)_2$, and $Ni(OH)_2 - H_2O \rightarrow NiO$.[30,31] The cathode surface was covered by numerous dendrites with massive micro-branches, while the anode was neat (Fig. S1 and S2†).

Fig. 1a shows the XRD pattern of the DNE material whose particle size is $\sim$4.8 nm (estimated by the Debye–Scherrer method). Three relatively strong diffraction peaks at 44.5°, 51.8° and 76.2° result from the cubic nickel (JCPDF 87-0712) deposited on the substrate. Compared with the bare Ni substrate, the electrodeposited DNE, consisting of crystallized Ni, showed preferred growth along the ⟨111⟩ direction, characteristic of the dendritic morphology of Ni.[32] The dendritic structure can also be easily identified from TEM (Fig. 1b), with micro- to nano-branches (Fig. 1c and S3†). The elemental mapping of Fig. 3b is shown in Fig. S4.† The high-resolution TEM (HRTEM) image (Fig. 1d) shows a *d*-spacing of 0.207 nm in the core of dendrites, corresponding to the interplanar distance of (111) planes of Ni and is consistent with the XRD results. In the corresponding selected area electron diffraction pattern (SAED, Fig. 1e), a distinct ring is observed, corresponding to the (111) plane of Ni nanocrystals.[33,34] The shell of dendrites is, however, amorphous. This core–shell structure is also verified by the fast Fourier transformation (FFT) patterns, as shown in Fig. 1f and g. EDS (Fig. S5†) reveals that the as-prepared dendrites contain both Ni and O elements, suggesting that the outer surface (shell) of the as-prepared dendrites is amorphous nickel oxide.

This core/shell structure was further studied by XPS. Fig. 2a shows the Ni 2p XPS spectrum with two shake-up satellites (denoted as Sat.) near the two spin–orbit doublets at 856.1 and 873.8 eV, which can be assigned to Ni $2p_{3/2}$ and Ni $2p_{1/2}$ signals of NiO, respectively.[35,36] In addition, another Ni $2p_{3/2}$ peak at 852.9 eV, corresponding to the Ni element,[37] can be identified. The atomic ratio of Ni^0 to Ni^{2+} was 1 : 10, as estimated from the peak areas. This result implies that the surface of dendrites mainly consists of NiO, as XPS normally probes a depth in the order of 10 nm.[38] An XPS depth profile (Fig. 2b) was carried out to verify the core/shell structure. A gradual increase in Ni and decrease in O with the profiling depth are observed (Fig. 2c), consistent with the Ni core and NiO shell structure. The XPS survey spectrum (Fig. S6†) shows no detectable signals other than Ni, O and adventitious carbon on the surface of the dendrites, indicating that no impurities were introduced during the electrodeposition. Fig. 2d shows the Raman spectra of the DNE, where the bands at 529.5 and 1078.1 cm^{-1} correspond to the one-phonon LO and the two-phonon 2LO modes of NiO, respectively,[39,40] confirming the existence of NiO.

Before the evaluation of the electrochemical performance of the DNE, the electrode was electrochemically activated in a three-electrode system in 1 mol L^{-1} NaOH aqueous electrolyte. A gradual increase of the current density with cycle number was observed (Fig. S7†). A distinctive pair of redox peaks between −0.2 and 0.65 V is due to the insertion/extraction of OH^- ions ($NiO + OH^- - e^- \rightleftharpoons NiOOH$),[41] illustrating the typical faradaic behaviour of the DNE.

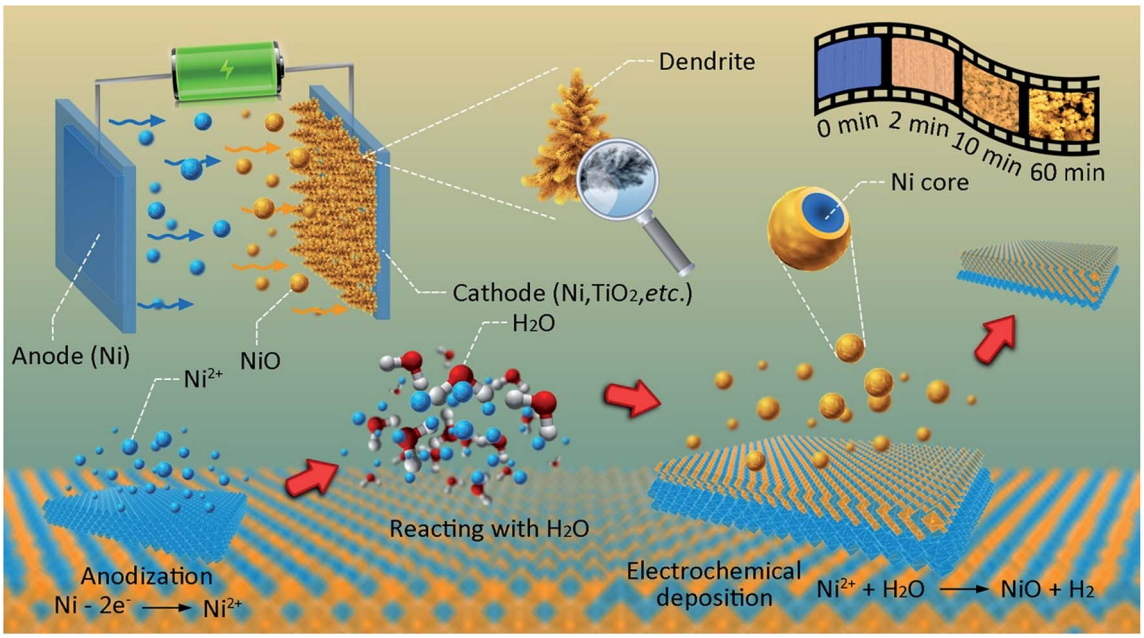

Scheme 1 Schematic illustration of the formation of the DNE material.

Fig. 3a shows the typical cyclic voltammetry (CV) curves of the as-prepared DNE after the electrochemical activation. With increasing scan rate, the current density increases accordingly, and there is no big change in the shape of CV curves, indicating that the DNE is a good conductor with a small equivalent series resistance (ESR) and excellent rate properties. The linear relationship between the cathodic peak current and the square root of the scan rate shows that the reaction process at the electrode was diffusion controlled rather than charge transfer limited. At a scan rate of 5 mV s^{-1}, the specific capacitance of the DNE calculated from CV is 1557 F g^{-1} (1.02 F cm^{-2}) (Fig. 3b), better than previous reports.[17,42,43] When the scan rate is increased to 100 mV s^{-1}, the DNE has a good rate capability with more than 60.7% retention of the capacitance (945 F g^{-1}, 0.66 F cm^{-2}).

The excellent electrochemical performance of the DNE was further confirmed by the galvanostatic charge–discharge (GCD) measurement (Fig. 3c). Charge/discharge plateaus in the GCD curves show strong faradaic behaviour, in agreement with the CV. At a current density of 2.9 A g^{-1} (2 mA cm^{-2}), the specific capacitance of the DNE is 1928.5 F g^{-1} (1.35 F cm^{-2}, calculated from the discharge curve). This value is superior to those of the reported state-of-the-art nickel-based electrodes (Table S1†). The high specific surface area (85.5 m^2 g^{-1}, Fig. S8†) of the DNE is one of the factors that contribute to this outstanding electrochemical performance. The rate capability of the DNE at different current densities is also good, with only 29.2% decay when the current is increased from 2.9 A g^{-1} to 58 A g^{-1} (Fig. S9†).

Electrochemical impedance spectroscopy (EIS) of the DNE (Fig. 3d) shows that the ESR (R_s) of the as-prepared DNE is about 1.4 Ω, indicative of a low electrolyte resistance and a low contact resistance between the active material and the current collector. The high frequency region of the EIS shows a depressed semicircle with a charge transfer resistance (R_{ct}) of 0.8 Ω (inset of Fig. 3d) that is much lower than those reported elsewhere,[17,44] implying a high power density. The low frequency portion of the EIS shows a straight line, representing the Warburg impedance, resulting from the ion diffusion/migration in the electrolyte. The large slope of the straight line indicates that the ion diffusion at the electrode–electrolyte interface was fast enough to catch up with the frequency change. The equivalent circuit of the DNE is shown in Fig. S10.†

Fig. 4a shows the variation of the gravimetric capacitance of the DNE in the cyclic test up to 70 000 cycles. During the first 800 cycles, the augmented specific capacitance was much greater than that at the first cycle (Fig. S7†). Notably, the capacitance continuously increased in the initial 20 000 cycles. From 20 000 to 60 000 cycles, there was no obvious drop in capacitance (945 F g^{-1}), demonstrating excellent electrochemical stability of the DNE. After 60 000 cycles, the capacitance is still 110% of the initial value (859 F g^{-1}), which slightly declines to 100% up to 70 000 cycles. To explore more details of the unique electrochemical reaction during cycling, CVs at different cycling stages are compared (Fig. 4b). After 800 cycles, the anodic peak potential shifted from 0.48 to 0.55 V, while the cathodic peak potential remained unchanged at 0.3 V. This phenomenon is attributed to the phase transition from γ-Ni(OOH) to β-Ni(OOH).[30,45–47]

The continuous increase in capacitance in the first 40 000 cycles is contradictory to the fact that β-Ni(OOH) has poorer electrochemical activity than γ-Ni(OOH).[30] We ascribe the increased capacitance to the gradual transition of the Ni core of the dendrites into β-Ni(OOH) during the cycling process,[48,49] resulting in exceptionally superior cycle life and good capacitance as compared with other recent reports.[17,50–52] This gradual transition of Ni into β-Ni(OOH) during cycling does not affect

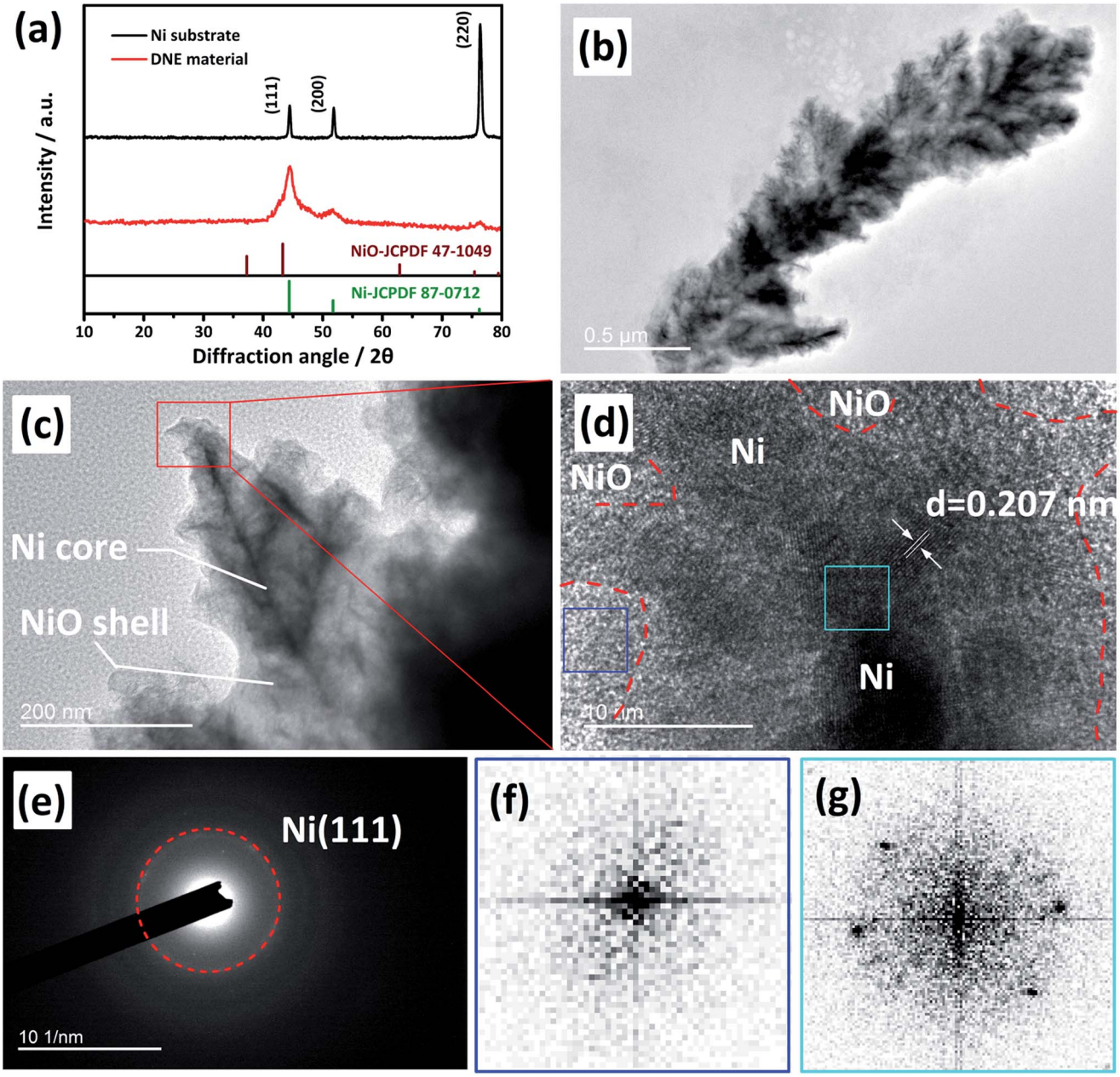

Fig. 1 Characterization of the DNE. (a) XRD. (b) Low and (c) high magnification TEM images. (d) HRTEM of the marked area of (c). Red dotted line is a guide to the eye to show roughly the Ni/NiO interface. (e) SAED pattern from (c). (f and g) Fast Fourier transformation (FFT) patterns of the marked areas of (d).

the coulombic efficiency or the rate capability too much (Fig. S11†).

Fig. 4c shows that the characteristic Raman peaks of NiO (LO and 2LO modes) can still be observed in the DNE after 800 cycles. After 8000 cycles, a new peak at 714.2 cm^{-1} can be found, which belongs to $Ni(OH)_2$ (ref. 53) due to the electrochemical oxidation of Ni, commonly found in alkaline electrolytes. Meanwhile, more and much stronger characteristic Raman peaks at 370.6, 506.7, 690.1 and 1078.1 cm^{-1} are found, which correspond to TO, 2TO and 2LO modes of NiO,[54] respectively, confirming the gradual transformation of the Ni core into electrochemically active NiO. The transformation of Ni into NiO and $Ni(OH)_2$ continues up to 40 000 cycles, as the intensities of the corresponding Raman peaks keep on increasing. After 70 000 cycles, however, the Raman peaks of $Ni(OH)_2$ disappeared and the intensities of the NiO peaks became remarkably weaker, indicating that the Ni core stopped its reaction with the electrolyte and the NiO and $Ni(OH)_2$ were partially dissolved in the electrolyte during repeated ion intercalation/deintercalation cycling. This result agrees with the cyclic test where the capacitance starts to decay after 70 000 cycles. Hence, the ultra-long cycle life of the DNE results from the continuous transformation of the newly exposed Ni core into NiO and $Ni(OH)_2$ during the cycling process.

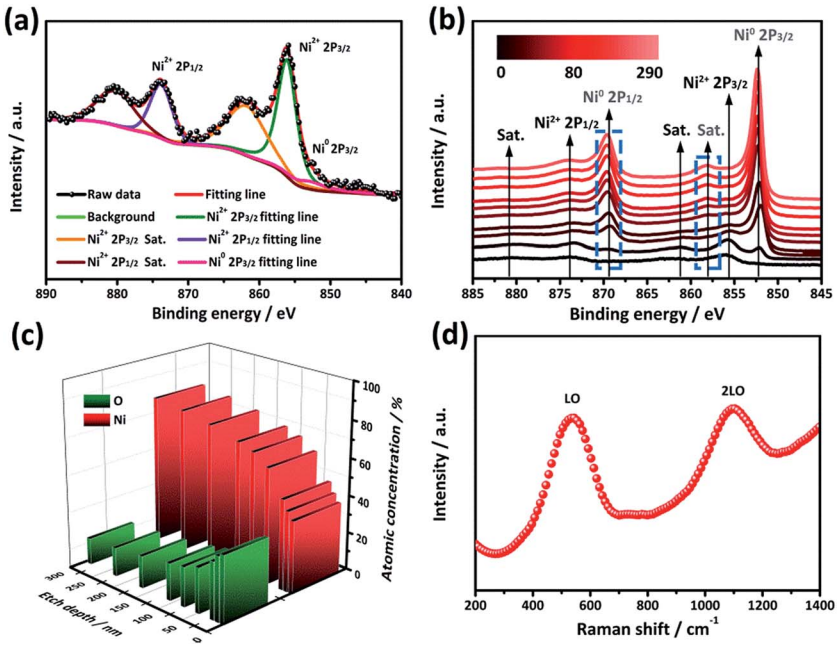

Fig. 2 (a) Ni 2p XPS on the fresh sample. (b) Depth profile of Ni 2p XPS on the DNE from 0 to 290 nm. (c) Variation of O and Ni concentrations as a function of the etch depth. (d) Raman spectrum of the DNE.

The dendritic core@shell morphology of the DNE (Fig. 4d and 5a) remains almost unchanged even after 70 000 cycles, revealing a remarkable structural stability. Moreover, partial transformation of the Ni core boundary into crystalline NiO that has a *d*-spacing of 0.147 nm corresponding to the interplanar distance of the (220) plane of NiO was also observed after 70 000 cycles (Fig. 5b and c). The corresponding SEAD pattern shows diffraction rings corresponding to the (111) and (220) planes of NiO nanocrystals. These results are consistent with the Raman spectra analysis.

It can be seen from the above results that the key to the superior electrochemical performance of the DNE is its unique dendritic core/shell microstructure, with the Ni core being a good conductor that shortens the ion diffusion path and the NiO shell possessing a large amount of electrochemically active sites for an excellent faradaic capacitance. Moreover, the gradual transformation of the Ni core into an electroactive material helps the DNE maintain an ultra-long cycle life. This unique microstructure results from the Ni-free electrolyte used in our work, where Ni^{2+} ions come from the Ni anode under potential or over-potential, different from previous work with

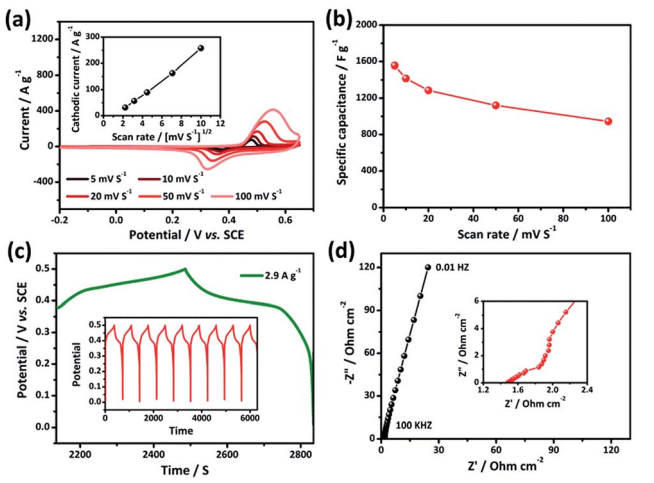

Fig. 3 Electrochemical characterization of the DNE. (a) CV curves at different scan rates. Inset: cathodic peak current as a function of the square root of the scan rate. (b) Specific capacitance at different scan rates. (c) GCD curves at 2.9 A g^{-1} (2 mA cm^{-2}). (d) EIS of the DNE from 0.01 to 100 kHz in 1 mol L^{-1} NaOH. Inset: magnified EIS in the high frequency region.

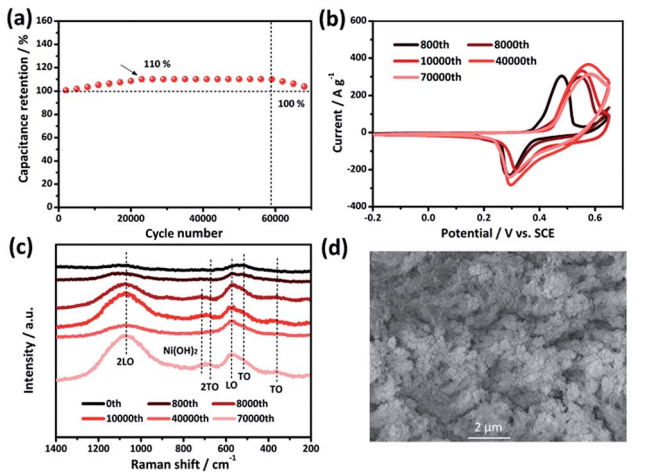

Fig. 4 (a) Cycling test of the DNE at a scan rate of 100 mV s^{-1}, (b) CV curves of the DNE at different cycle numbers at a scan rate of 100 mV s^{-1}, (c) Raman spectra of the DNE at different cycle numbers, and (d) SEM image of the DNE after 70 000 cycles.

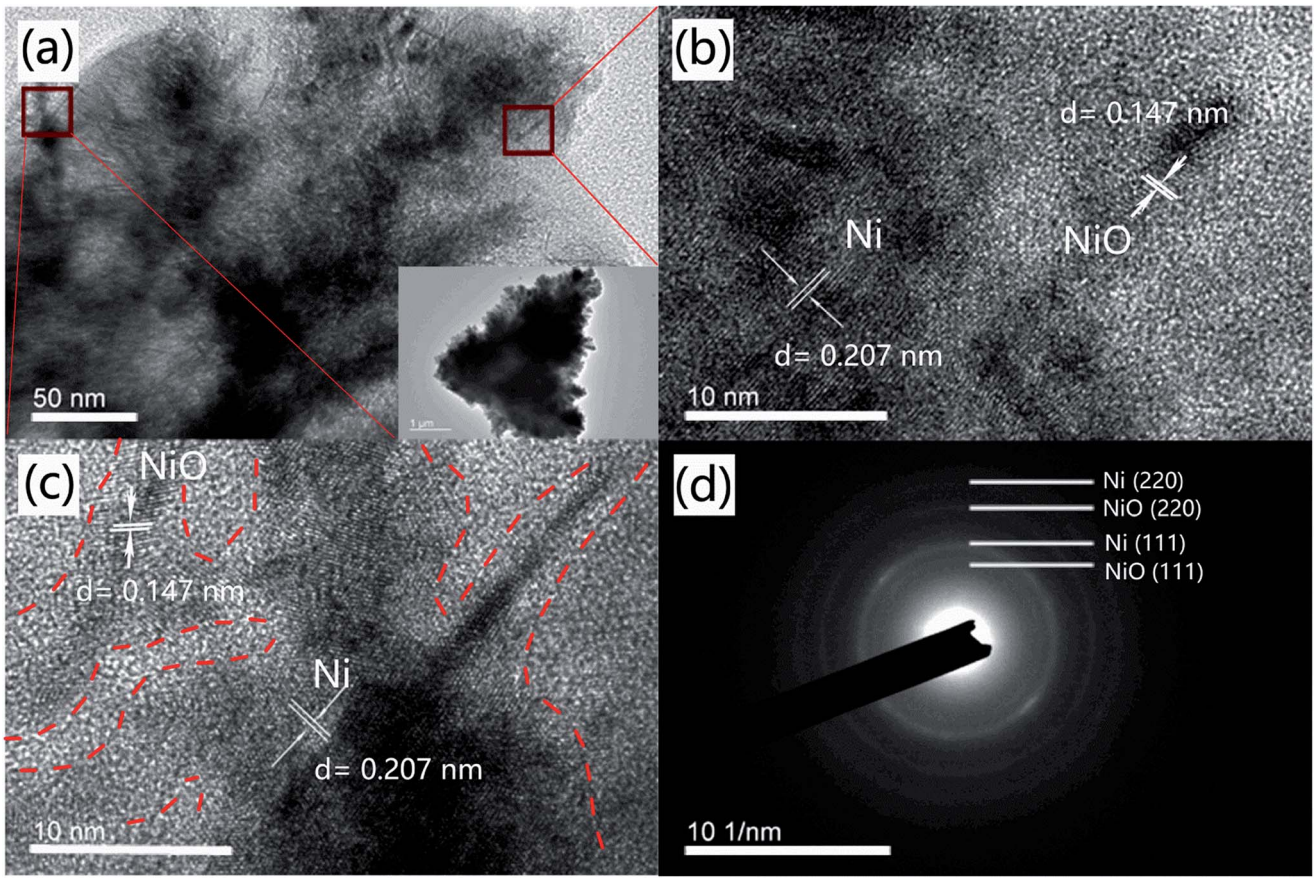

Fig. 5 (a) High and low (the inset) magnification TEM images of the DNE material after 70 000 cycles. (b and c) HRTEM image of the marked areas in (a). (d) SEAD pattern. Red dotted line is a guide to the eye to show roughly the boundary between crystalline and amorphous phases.

a Ni^{2+}-containing electrolyte as the only Ni source for electrodeposition.[55] In this study, a viscous organic electrolyte (EG) was used to control the diffusion of Ni^{2+} (ref. 29 and 56) in order to get a steady deposition on the cathode for the formation of the dendritic DNE. A small amount of water is necessary for the reduction of Ni^{2+} and the deposition of Ni on the cathode. As water was gradually depleted, the local pH increased and the surface of the electrode was gradually passivated, forming a layer of oxide or hydroxide[30,57,58] to cover the Ni core. Thus, the dendritic Ni@NiO core/shell structure was finally formed.

Similar to the preferential free growth of dendrite silver or platinum,[59] which was driven by overpotential or thermal undercooling, the dendritic Ni core also grew along the ⟨111⟩ direction (Fig. 1). In the electrodeposition of nickel, dendrite growth along the preferred orientation frequently occurs under high current density or overpotential.[60,61] Among the many factors that control the dendrite growth, the most important one is the H^+ ions from water electrolysis, whose content and migration rate affect metallic overpotential and thus the nucleation rate.[62] It is well known that the hydrogen evolution reaction (HER) involving an intermediate H adsorption could make an important contribution to the preferential oriented growth.[56,63] At the cathode, H^+ is slowly consumed by hydrogen evolution. Reddy *et al.* proposed that the change of nickel texture is induced by variation in surface hydrogen adsorption which depends on temperature, additive and current density.[62] Since temperature affects the diffusion of Ni^{2+} and H^+, and the viscosity of the electrolyte, to elucidate the effect of temperature on the growth of dendrites, several different temperatures were tried. The electrodeposition current was the most stable at 40 °C under an applied voltage of 60 V (Fig. S12†), indicating steady ion diffusion and migration. The stable current density ensures a stable hydrogen evolution and bubbles can be observed on the surface of the cathode. Since the growth of the dendritic DNE depends on the kinetic equilibrium of nickel dissolution, dissociation of DI water, hydrogen evolution and nickel deposition, the use of viscous EG could keep smooth and stable migration of Ni^{2+}, OH^- and H^+, as well as proper hydrogen evolution. In order to elucidate the effect of electrolyte, different electrolytes were also tried. When EG was replaced by DI water and/or $Ni(Ac)_2$, the as-prepared samples showed poor electrochemical performances (Fig. S13†). As shown in Fig. S14,† when the balance between the migration of Ni^{2+}, OH^- and H^+ ions and the generation of H_2 was disturbed, either the excess H_2 on the cathode caused vigorous formation of H_2 bubbles, which seriously degraded the adhesion of the active material on the electrode (the red line), or the gradually exhausted Ni^{2+} ions (in $Ni(Ac)_2$ electrolyte) could not maintain the steady formation of Ni@NiO (the black line). Similar to the cases in previous reports, the as-obtained materials were made up of numerous

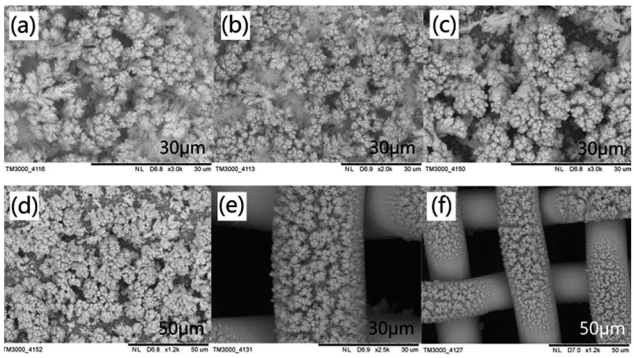

Fig. 6 Surface morphologies of the electrodeposited cathodes at 40 °C on (a and b) Fe foil, (c and d) TiO_2 nanotube array, and (e and f) stainless steel net.

flakes or particles (Fig. S15†) and showed poor cycle life (Fig. S16†). Besides, the water content also affects the amount of H^+ ions and ion diffusion in the viscous electrolyte. Our results showed that the sample prepared in the electrolyte of 3 vol% water exhibited the best electrochemical performance (Fig. S17†). NH_4F also played an important role in the electrochemical deposition (Fig. S18†). When NH_4F was replaced by NH_4Cl, the formation of the active materials was difficult. Additionally, the deposition time also affects the electrochemical performance of the electrodes (Fig. S19†). A too-short or too-long deposition time is detrimental to the specific capacitance of the electrodes, with 1 hour being the optimum deposition time for the growth of a well-developed dendritic structure with a slim enough yet interconnected Ni core.

At different stages of electrodeposition (Fig. S20†), the deposited material experienced three levels of structural evolution, from nanoneedles to microbranches and finally to dendrites.

It is also interesting to note that such a dendritic morphology can be obtained by electrodeposition on not only Ni foil, but also other substrates, such as, stainless steel plates, TiO_2 nanotube arrays, and stainless steel nets (Fig. 6). This indicates that our electrodeposition method (in Ni-free electrolyte) is universal to deposit dendritic Ni-compounds on many types of substrates, versatile for different applications.

Conclusions

In summary, a dendritic Ni@NiO core/shell electrode is fabricated by one-step electrodeposition in a source-free electrolyte. The unique architecture of the DNE results in excellent gravimetric capacitance (1930 F g^{-1} at 2.9 A g^{-1}), high rate capability and ultra-long cycle life (100% after 70 000 cycles), showing great potential for energy storage applications. Our method may also be extended to other metal systems, such as $Co@Co_2O_3$ and $Fe@Fe_2O_3$ for the exploration of high capacity EESDs.

Acknowledgements

This work was supported by the Research Grants Council of the Hong Kong Special Administrative Region, China (Project No. M-PolyU503/13, PolyU5163/12E and PolyU5159/13E) and the Hong Kong Polytechnic University (Project No. 1-ZVGH).

References

1 M. Yu, Z. Wang, Y. Han, Y. Tong, X. Lu and S. Yang, *J. Mater. Chem. A*, 2016, **4**, 4634–4658.
2 H. Wang, H. S. Casalongue, Y. Liang and H. Dai, *J. Am. Chem. Soc.*, 2010, **132**, 7472–7477.
3 J. Yan, Z. Fan, W. Sun, G. Ning, T. Wei, Q. Zhang, R. Zhang, L. Zhi and F. Wei, *Adv. Funct. Mater.*, 2012, **22**, 2632–2641.
4 Y. Bai, M. Du, J. Chang, J. Sun and L. Gao, *J. Mater. Chem. A*, 2014, **2**, 3834–3840.
5 Y. Fu, J. M. Song, Y. Q. Zhu and C. B. Cao, *J. Power Sources*, 2014, **262**, 344–348.
6 F. Yang, J. Y. Yao, F. L. Liu, H. C. He, M. Zhou, P. Xiao and Y. H. Zhang, *J. Mater. Chem. A*, 2013, **1**, 594–601.
7 J. W. Zhu, S. Chen, H. Zhou and X. Wang, *Nano Res.*, 2012, **5**, 11–19.
8 B. Wang, J. S. Chen, Z. Y. Wang, S. Madhavi and X. W. Lou, *Adv. Energy Mater.*, 2012, **2**, 1188–1192.
9 M. Khairy and S. A. El-Safty, *Sens. Actuators, B*, 2014, **193**, 644–652.
10 E. Umeshbabu, G. Rajeshkhanna and G. R. Rao, *Int. J. Hydrogen Energy*, 2014, **39**, 15627–15638.
11 H. Wu, K. Jiang, S. Gu, H. Yang, Z. Lou, D. Chen and G. Shen, *Nano Res.*, 2015, **8**, 3544–3552.
12 T.-Y. Wei, C.-H. Chen, H.-C. Chien, S.-Y. Lu and C.-C. Hu, *Adv. Mater.*, 2010, **22**, 347–351.
13 S. I. Kim, J. S. Lee, H. J. Ahn, H. K. Song and J. H. Jang, *ACS Appl. Mater. Interfaces*, 2013, **5**, 1596–1603.
14 A. K. Singh, D. Sarkar, G. G. Khan and K. Mandal, *ACS Appl. Mater. Interfaces*, 2014, **6**, 4684–4692.
15 Q. Lu, M. W. Lattanzi, Y. Chen, X. Kou, W. Li, X. Fan, K. M. Unruh, J. G. Chen and J. Q. Xiao, *Angew. Chem., Int. Ed.*, 2011, **50**, 6847–6850.
16 H. Lai, Q. Wu, J. Zhao, L. Shang, H. Li, R. Che, Z. Lyu, J. Xiong, L. Yang, X. Wang and Z. Hu, *Energy Environ. Sci.*, 2016, **9**, 2053–2060.
17 G. G. Zhang, W. F. Li, K. Y. Xie, F. Yu and H. T. Huang, *Adv. Funct. Mater.*, 2013, **23**, 3675–3681.
18 M. Jin, G. Zhang, F. Yu, W. Li, W. Lu and H. Huang, *Phys. Chem. Chem. Phys.*, 2013, **15**, 1601–1605.
19 J. Hu, M. Li, F. Lv, M. Yang, P. Tao, Y. Tang, H. Liu and Z. Lu, *J. Power Sources*, 2015, **294**, 120–127.
20 C. Shang, S. Dong, S. Wang, D. Xiao, P. Han, X. Wang, L. Gu and G. Cui, *ACS Nano*, 2013, **7**, 5430–5436.
21 S. W. Chou and J. Y. Lin, *J. Electrochem. Soc.*, 2013, **160**, D178–D182.
22 M. Yang, H. Cheng, Y. Gu, Z. Sun, J. Hu, L. Cao, F. Lv, M. Li, W. Wang, Z. Wang, S. Wu, H. Liu and Z. Lu, *Nano Res.*, 2015, **8**, 2744–2754.
23 J.-C. Chen, C.-T. Hsu and C.-C. Hu, *J. Power Sources*, 2014, **253**, 205–213.
24 F. Cao, G. X. Pan, X. H. Xia, P. S. Tang and H. F. Chen, *J. Power Sources*, 2014, **264**, 161–167.

25 C.-H. Lien, C.-C. Hu, C.-T. Hsu and D. S.-H. Wong, *Electrochem. Commun.*, 2013, **34**, 323–326.
26 L. K. Wu, J. M. Hu, J. Q. Zhang and C. N. Cao, *J. Mater. Chem. A*, 2013, **1**, 12885–12892.
27 H. Yi, X. Chen, H. W. Wang and X. F. Wang, *Electrochim. Acta*, 2014, **116**, 372–378.
28 D. T. Dam, X. Wang and J. M. Lee, *Nano Energy*, 2013, **2**, 1303–1313.
29 H. B. Li, M. H. Yu, F. X. Wang, P. Liu, Y. Liang, J. Xiao, C. X. Wang, Y. X. Tong and G. W. Yang, *Nat. Commun.*, 2013, **4**, 1894–1900.
30 Y. L. Lo and B. J. Hwang, *Langmuir*, 1998, **14**, 944–950.
31 Y. Zhao, L. Hu, S. Zhao and L. Wu, *Adv. Funct. Mater.*, 2016, **26**, 4038.
32 C. H. Lien, C. C. Hu, Y. D. Tsai and D. S. H. Wang, *J. Electrochem. Soc.*, 2012, **159**, D260–D264.
33 Z. Pi, T. Tian, X. Tian, C. Yang, S. Zhang and J. Zheng, *J. Nanosci. Nanotechnol.*, 2007, **7**, 673–676.
34 X. Xia, J. Tu, Y. Zhang, X. Wang, C. Gu, X. B. Zhao and H. J. Fan, *ACS Nano*, 2012, **6**, 5531–5538.
35 A. N. Mansour, *Surf. Sci. Spectra*, 1994, **3**, 231–238.
36 J. A. Schreifels, P. C. Maybury and W. E. Swartz Jr, *J. Catal.*, 1980, **65**, 195–206.
37 D. Chadwick and T. Hashemi, *Corros. Sci.*, 1978, **18**, 39–51.
38 W. T. Becker and R. J. Shipley, *Failure Analysis and Prevention*, ASM International, UC, CA, USA, 2002.
39 N. Mironova-Ulmane, A. Kuzmin, I. Steins, J. Grabis, I. Sildos and M. Pärs, *J. Phys.: Conf. Ser.*, 2007, **93**, 012039–012043.
40 A. C. Gandhi, C. Y. Huang, C. C. Yang, T. S. Chan, C. L. Cheng, Y. R. Ma and S. Y. Wu, *Nanoscale Res. Lett.*, 2011, **6**, 485–498.
41 T. Gao and B. P. Jelle, *J. Phys. Chem. C*, 2013, **117**, 17294–17302.
42 Z. Tang, C. H. Tang and H. Gong, *Adv. Funct. Mater.*, 2012, **22**, 1272–1278.
43 P. Lin, Q. J. She, B. L. Hong, X. A. J. Liu, Y. N. Shi, Z. Shi, M. S. Zheng and Q. F. Dong, *J. Electrochem. Soc.*, 2010, **157**, A818–A823.
44 X. Cao, Y. Shi, W. Shi, G. Lu, X. Huang, Q. Yan, Q. Zhang and H. Zhang, *Small*, 2011, **7**, 3163–3168.
45 D.-B. Kuang, B.-X. Lei, Y.-P. Pan, X.-Y. Yu and C.-Y. Su, *J. Phys. Chem. C*, 2009, **113**, 5508–5513.
46 M. Wehrens-Dijksma and P. H. L. Notten, *Electrochim. Acta*, 2006, **51**, 3609–3621.
47 H. Bode, K. Dehmelt and J. Witte, *Electrochim. Acta*, 1966, **11**, 1079–1087.
48 X. Dai, D. Chen, H. Q. Fan, Y. Zhong, L. Chang, H. B. Shao, J. M. Wang, J. Q. Zhang and C. N. Cao, *Electrochim. Acta*, 2015, **154**, 128–135.
49 M. H. Yu, W. Wang, C. Li, T. Zhai, X. H. Lu and Y. X. Tong, *NPG Asia Mater.*, 2014, **6**, e129–e136.
50 H. Chen, L. Hu, M. Chen, Y. Yan and L. Wu, *Adv. Funct. Mater.*, 2014, **24**, 934–942.
51 S. Chen, J. Duan, Y. Tang and S. Zhang Qiao, *Chemistry*, 2013, **19**, 7118–7124.
52 H. Chen, L. F. Hu, Y. Yan, R. C. Che, M. Chen and L. M. Wu, *Adv. Energy Mater.*, 2013, **3**, 1636–1646.
53 C. Johnston and P. Graves, *Appl. Spectrosc.*, 1990, **44**, 105–115.
54 W. Z. Wang, Y. K. Liu, C. K. Xu, C. L. Zheng and G. H. Wang, *Chem. Phys. Lett.*, 2002, **362**, 119–122.
55 C. C. Hu, J. C. Chen and K. H. Chang, *J. Power Sources*, 2013, **221**, 128–133.
56 A. K. N. Reddy and S. K. Rajagopalan, *J. Electroanal. Chem.*, 1963, **6**, 153–158.
57 I. Epelboin, M. Joussellin and R. Wiart, *J. Electroanal. Chem.*, 1981, **119**, 61–71.
58 T. Pauporté, A. Goux, A. Kahn-Harari, N. De Tacconi, C. Chenthamarakshan, K. Rajeshwar and D. Lincot, *J. Phys. Chem. Solids*, 2003, **64**, 1737–1742.
59 J. Barton and J. M. Bockris, *Proc. R. Soc. London, Ser. A*, 1962, **268**, 485–505.
60 K. Zhuo, M. G. Jeong and C. H. Chung, *RSC Adv.*, 2013, **3**, 12611–12615.
61 S. Eugénio, T. M. Silva, M. J. Carmezim, R. G. Duarte and M. F. Montemor, *J. Appl. Electrochem.*, 2013, **44**, 455–465.
62 A. K. N. Reddy, *J. Electroanal. Chem.*, 1963, **6**, 141–152.
63 A. K. N. Reddy and S. R. Rajagopalan, *J. Electroanal. Chem.*, 1963, **6**, 159–163.

